ELSEVIER

Journal of Nuclear Materials 257 (1998) 21–34

journal of nuclear materials

Evaluation of stainless steel–zirconium alloys as high-level nuclear waste forms

S.M. McDeavitt *, D.P. Abraham, J.Y. Park

Chemical Technology Division, Argonne National Laboratory, Building 205, 9700 South Cass Avenue, Argonne, IL 60439-4837, USA

Received 26 September 1997; accepted 5 May 1998

Abstract

Stainless steel–zirconium (SS–Zr) alloys have been developed for the consolidation and disposal of waste stainless steel, zirconium, and noble metal fission products such as Nb, Mo, Tc, Ru, Pd, and Ag recovered from spent nuclear fuel assemblies. These remnant waste metals are left behind following electrometallurgical treatment, a molten salt-based process being demonstrated by Argonne National Laboratory. Two SS–Zr compositions have been selected as baseline waste form alloys: (a) stainless steel–15 wt% zirconium (SS–15Zr) for stainless steel-clad fuels and (b) zirconium–8 wt% stainless steel (Zr–8SS) for Zircaloy-clad fuels. Simulated waste form alloys were prepared and tested to characterize the metallurgy of SS–15Zr and Zr–8SS and to evaluate their physical properties and corrosion resistance. Both SS–15Zr and Zr–8SS have multi-phase microstructures, are mechanically strong, and have thermophysical properties comparable to other metals. They also exhibit high resistance to corrosion in simulated groundwater as determined by immersion, electrochemical, and vapor hydration tests. Taken together, the microstructure, physical property, and corrosion resistance data indicate that SS–15Zr and Zr–8SS are viable materials as high-level waste forms.

PACS: 28.41.Kw; 81.05.Bx; 81.20-q; 61.66.Dk

1. Introduction

The term waste form refers to 'radioactive waste materials and any encapsulating or stabilizing matrix' that will ultimately be placed into a 'waste package' for disposal [1,2]. A number of waste form materials have been developed for various applications, and comprehensive reviews of their characteristics and behavior are available [3–8]. The most prevalent waste form technology is vitrification in borosilicate glass, but other materials are being investigated at a less extensive level of effort (e.g., phosphate glasses, glass ceramics, and custom ceramics such as Synroc) [3,4]. In addition, spent nuclear fuel assemblies are considered complete, self-contained waste forms in several countries [3,4]. At Argonne National Laboratory (ANL), stainless steel–zinconium (SS–Zr) waste form alloys have been developed for the express purpose of immobilizing radioactive metal fuel components left behind following the electrometallurgical treatment of spent nuclear fuel [9–14]. Previous reports regarding the SS–Zr waste forms have described the metal waste stream from electrometallurgical treatment [9–11], microstructural characterization of SS–Zr alloys [10–14], and preliminary test results from corrosion experiments and property measurements [11–13].

The electrometallurgical treatment process is being developed at ANL to stabilize 'at-risk' spent fuel types that are not suitable for direct repository disposal and may not be directly processed using existing aqueous methods [15–20]. This process was originally developed to treat fast reactor fuel alloys [16–18], but it has since evolved into a waste treatment method [15,19–22]. The first fuel to be treated using this process will be the so-

* Corresponding author. Tel.: +1-630 252 4308; fax: +1-630 252 5246; e-mail: mcdeavitt@cmt.anl.gov.

0022-3115/98/$ – see front matter
PII: S0022-3115(98)00433-4

dium-bonded U–10 wt% Zr alloy (driver) and U metal (blanket) fuels from the Experimental Breeder Reactor-II (EBR-II). A full-scale demonstration using EBR-II spent fuel is presently underway at the Fuel Conditioning Facility (FCF) at ANL-West located near Idaho Falls, ID, USA [20].

Electrometallurgical treatment comprises a set of operations designed to break down spent nuclear fuel, recover refined uranium metal, and segregate the radioactive waste constituents into two waste forms: a glass–ceramic composite [21–25] and the SS–Zr alloy described here. The key operation in the process is the electrorefining of uranium metal in a molten salt electrolyte ($LiCl–KCl–UCl_3$). During this operation, the fuel is electrochemically dissolved, and uranium metal is deposited on a cathode. Transuranic actinides (e.g., Pu, Np, and Am), active fission products (e.g., Cs, Sr, and I), and rare earth fission products (e.g., Ce, Nd, and Pr) are oxidized by the electrolyte to form soluble chlorides. The salt-borne wastes are immobilized in zeolite through ion exchange and salt occlusion, and the loaded zeolite is processed into a glass–ceramic composite waste form [21–25].

The metal waste stream comprises remnant metallic constituents that are electrochemically noble (inert) in the electrorefiner that are collected for conversion into SS–Zr alloy waste forms. This collection of wastes includes cladding hulls from the spent fuel assemblies (which may be stainless steel or Zircaloy), noble metal fission products (NMFPs) (e.g., Ru, Rh, Pd, Nb, Mo, and Tc), and, in some cases, zirconium metal from alloy nuclear fuels. Handling this waste stream is complicated by the fact that the metals are covered with clinging salt from the electrorefiner that must be removed by distillation.

Since cladding hulls represent 85–99 wt% of the waste stream for all fuel types being evaluated for treatment, SS–Zr alloy waste forms were selected to blend the waste stream components with minimal alloying additions [11]. The conversion of the waste constituents into SS–Zr waste forms is accomplished by melting and alloying the metal wastes together in a high-temperature, inert-atmosphere furnace. Two SS–Zr compositions were selected as baseline waste form alloys: (a) stainless steel–15 wt% zirconium (SS–15Zr) for stainless steel-clad fuel and (b) Zircaloy–8 wt% stainless steel (Zr–8SS) for Zircaloy-clad fuel [11].

Because of the abundance of characterization and performance data for borosilicate glass, Synroc, and other waste form materials [3,4], one might question the need to develop a completely different waste form technology using new, unproven materials. Acid-stripping the cladding, vitrification of the subsequent liquid waste, and compaction of decontaminated cladding are established technologies [4,6,26–28]. However, the development of the SS–Zr waste forms was necessary because of the unique characteristics of the electrometallurgical process and its waste stream. Metal matrix encapsulation was evaluated for electrorefiner metal wastes in parallel to the early development of the SS–Zr alloys [9], but alloying was selected over encapsulation because of superior behavior of the waste form.

The decision to avoid vitrification was based on practical and technical considerations. One early design criterion was that the waste treatment technology must be compact and compatible with the process environment [21]. Salt distillation and alloying of the waste components may be accomplished in a high-temperature furnace with a salt recovery mechanism. This is a simple, one-step process and the product is a waste form suitable for geologic disposal, as discussed in this paper. In addition, there are at least two technical issues which make vitrification of this waste stream undesirable. First, the NFMPs, or platinoids, are strong crystal formers in vitrified waste forms, and crystal formation decreases the mechanical integrity of glass [3,6,8,26,27]. In other words, the primary radioactive isotopes in the metal waste stream are generally incompatible with glass. Second, direct vitrification of the metallic wastes would result in significant mass and volume increases [12,27] since the metals must be oxidized and combined with significant quantities of glass-forming materials prior to vitrification.

The development of a new waste form material requires thorough evaluation of its physical attributes (i.e., microstructure and physical properties) and characterization of its alteration (or corrosion) behavior in a geologic repository environment. As a first step toward establishing SS–15Zr and Zr–8SS as viable waste form materials, small- and large-scale alloy specimens ($\sim$10 g to $\sim$3 kg) have been evaluated by a variety of methods. The alloy metallurgy has been examined by means of scanning electron microscopy (SEM), energy dispersive spectroscopy (EDS), X-ray diffraction, and neutron diffraction. The corrosion behavior has been characterized using general immersion, electrochemical linear polarization, and accelerated test methods. Mechanical and thermophysical properties were also measured. This paper summarizes and updates previously reported data [10–13] and presents new data regarding fission product distribution and corrosion. In addition, the viability of SS–15Zr and Zr–8SS as high-level waste forms will be discussed in the context of the data that have been generated.

2. Equipment and methods

Small-scale alloys, between 10 and 30 g, were generated in a high-temperature, tungsten-element furnace. The furnace system was described by Abraham et al. [10], and it consists of a high-temperature vacuum fur-

Table 1
Composition of observed phases in stainless steel–15 wt% zirconium alloys [11,12] [a]

Phase	Crystal structure	Fe	Zr	Cr	Ni
α-Fe	Body-centered cubic	69	0	24	4
γ-Fe	Face-centered cubic	70	0	20	8
$Zr(Fe,Cr,Ni)_{2+x}$	$MgNi_2$-type & $MgCu_2$-type	54	24	8	11
Zr_6Fe_{23}-type	Th_6Mn_{23}-type	57	19	10	9

[a] Listed compositions are in atom% (±3%).

nace and a controlled-atmosphere specimen chamber made from Mo–30 wt% W that is inserted into furnace. Alloy samples were melted in yttrium oxide crucibles under a flowing argon atmosphere at 1600°C for 1 to 2 h and cooled slowly (~7°C/min). Alloys made with this cooling rate will be referred to as 'as cooled'. A typical specimen size was ~15 mm diameter by 30 to 40 mm tall. Small-scale specimens were used to investigate the metallurgy and corrosion behavior of SS–Zr alloys.

Large-scale alloys, between 1 and 3 kg, were generated in a tilt-pour induction furnace connected to an inert atmosphere glovebox. The furnace (design and fabrication by Thermal Technology, Concord, NH, USA) consists of two hot-zones within a water-cooled, stainless steel chamber, as described by McDeavitt et al. [29]. The melting furnace is a tilt-pour induction unit with a maximum rated temperature of 2200°C. An yttrium oxide crucible (~100 mm diameter and ~160 mm tall) is used to contain the melt. The crucible sits inside of a graphite susceptor and a retractable graphite lid is placed over the crucible. The lower furnace is a graphite element resistance unit that is used for preheating casting molds with a maximum temperature of 1600°C. Ingots furnace-cooled in the yttria crucible were ~10 cm in diameter and ~8 cm tall, whereas the shape of cast ingots was dependent upon the casting mold design, either a single slug of metal (~80 mm dia) or four rods (~30 mm dia each) connected by a small riser. The large-scale ingots were machined into specimens for microstructural examination, corrosion testing, and determination of their mechanical and thermophysical properties.

Alloy microstructures were characterized using a JEOL [1] 6400 SEM operating in both secondary and backscatter modes. Standardless quantitative analysis of the individual phases was obtained with an EDS spectrometer and Voyager II software from Noran Instruments (Middletown, WI). The crystal structures of the observed phases were determined by X-ray diffraction and neutron diffraction. X-ray diffraction data were collected on a Philips [2] powder diffractometer using CuK_α radiation. Time-of-flight neutron powder diffraction data were collected using the General Purpose Powder Diffractometer (GPPD) at the Intense Pulsed Neutron Source (IPNS) located at Argonne National Laboratory, Argonne, IL [30,31].

[1] JEOL is a trademark of Japan Electron Optics Ltd., Tokyo.

[2] Philips is a trademark of Philips Electronic Instruments Corp., Mahwah, NJ.

3. Metallurgy of stainess steel–zirconium alloys

3.1. Stainless steel–15 wt% zirconium

Large- and small-scale SS–15Zr specimens were generated using stainless steel Types 316, 304 [10], and HT9 [9] combined with high purity zirconium metal; the majority of the data and all large-scale specimens were generated using Type 316 stainless steel. The compositions and crystal structures of phases present in SS–15Zr alloys are summarized in Table 1, and a representative microstructure from an as-cooled SS–15Zr alloy is shown in Fig. 1. As a first approximation, the SS–15Zr alloy exhibits a eutectic structure containing an Fe solid solution phase (dark contrast) and a Laves-type intermetallic phase (bright contrast) designated as $Zr(Fe,Cr,Ni)_{2+x}$ [10–14,29–31]. This eutectic behavior is consistent with the Fe–Zr binary phase diagram in Fig. 2, which shows a similar eutectic at 1325°C between Fe and $ZrFe_2$. The Fe–Zr binary phase diagram is a useful, but simplified, guide for the discussion of the SS–Zr alloys; Fig. 2 is based on the most recent phase diagram reported by Arias et al. [32].

For SS–Zr alloy made with austentic 316 or 304 stainless steels, the Fe solution phase is typically a mixture of ferritic iron (α-Fe) and austenitic iron (γ-Fe), with Cr and Ni contents similar to those of ferritic and austenitic stainless steels (Table 1). The relative abundance of α-Fe vs γ-Fe depends on the Ni content in the starting stainless steel and the Zr content of the SS–Zr alloy. Below 15 wt% Zr, the Fe solution phase is a mixture of α-Fe and γ-Fe. At ~15 wt% Zr, near the eutectic composition, the Fe solution phase is essentially 100% α-Fe; the complete formation of α-Fe depends on the Zr and Ni content in the sample. Well above 15 wt% Zr, γ-Fe is not observed, and the relative $Zr(Fe,Cr,Ni)_{2+x}$ quantity increases until the Zr content exceeds ~40 wt% Zr, where only multicomponent intermetallic compounds are observed [10]. Alloys made using the ferritic HT9 stainless steel do not contain

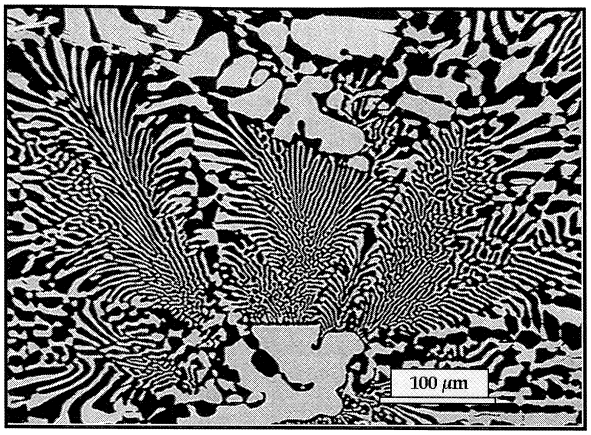

Fig. 1. Backscattered electron image of as-cooled stainless steel–15 wt% zirconium. The image reveals a eutectic microstructure containing an iron solid solution (dark) and the $Zr(Fe,Cr,Ni)_{2+x}$ intermetallic (bright).

γ-Fe, and the $Zr(Fe,Cr,Ni)_{2+x}$ phase is essentially $Zr(Fe,Cr)_{2+x}$.

The $Zr(Fe,Cr,Ni)_{2+x}$ Laves intermetallic is the multicomponent analog of $ZrFe_2$ from the binary phase diagram. Laves phases are a family of compounds with the general formula AB_2 and may have one or more of the following crystal structures: hexagonal $MgZn_2$-type (C14), cubic $MgCu_2$-type (C15), and dihexagonal $MgNi_2$-type (C36) [33–35]. Abraham et al. [31] used neutron diffraction to examine the structure of this in-

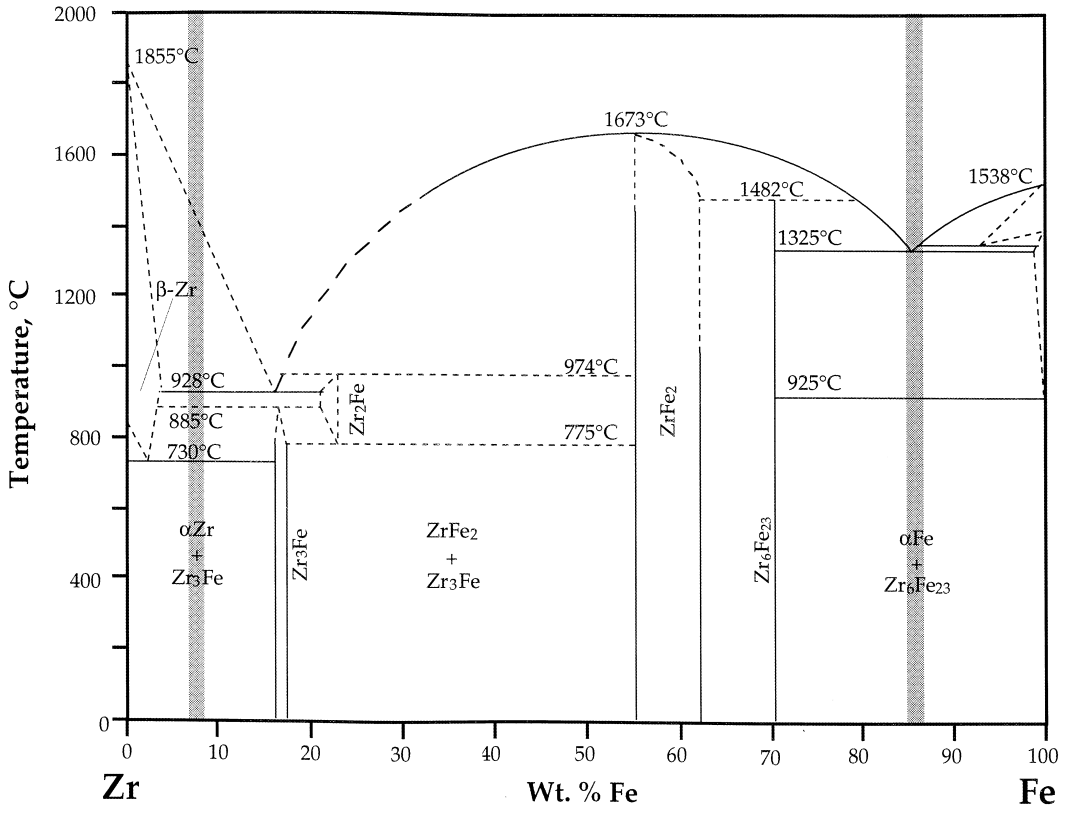

Fig. 2. Representation of the Fe–Zr binary phase diagram based on Ref. [32]. The highlighted compositions represent the binary complements to SS–15Zr and Zr–8SS.

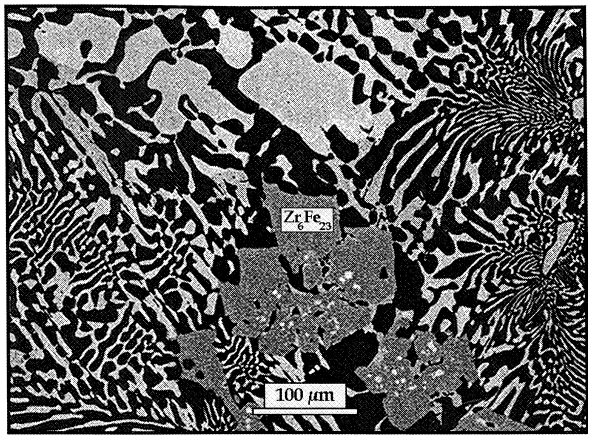

Fig. 3. Backscattered electron image of annealed stainless steel–15 wt% zirconium. The Zr_6Fe_{23} intermetallic content increases as annealing proceeds.

termetallic and found that the C36 and C15 Laves polytypes are the dominant structures in SS–15Zr, but a transition to C14 was observed as the Zr content increased.

A second Zr–Fe compound, $Zr_6(Fe,Cr,Ni)_{23}$, is also present in SS–15Zr [11,12,29–31]. This compound is analogous to the Zr_6Fe_{23} phase indicated in Fig. 2 as the equilibrium phase; Zr_6Fe_{23} has previously been mistakenly identified as $ZrFe_3$, as noted by Abraham et al. [30,31] and Liu et al. [36]. Recent experiments show that the formation of this phase is kinetically slow in SS–Zr and Fe–Zr alloys, but a minor fraction (typically between 1 and 5 vol.%) is present in as-cooled SS–15Zr alloys. After an SS–15Zr alloy was annealed at 1275°C for 2 h, the $Zr_6(Fe,Cr,Ni)_{23}$ content increased to 11 vol.%. A representative annealed structure from a SS–15Zr alloy is shown in Fig. 3; it contains α-Fe, $Zr(Fe,Cr,Ni)_{2+x}$, and the $Zr_6(Fe,Cr,Ni)_{23}$ intermetallic. The structure in Fig. 3 not yet at equilibrium; longer-term annealing tests up to 30 h have resulted in more than 30 vol.% $Zr_6(Fe,Cr,Ni)_{23}$ in the microstructure. The most stable form of this alloy apparently contains a 3-phase mixture of the α-Fe solution, the C15 Laves phase, and the $Zr_6(Fe,Cr,Ni)_{23}$ phase (determined by annealing and neutron diffraction experiments); γ-Fe and the C36 Laves intermetallic disappear upon extended annealing.

3.2. Zirconium–8 wt% stainless steel

Large- and small-scale Zr–8SS specimens were generated using high purity zirconium metal and Type 304 stainless steel [10–12]. The compositions and crystal structures for the observed phases in Zr–8SS alloys are summarized in Table 2 (as determined by EDS and X-ray diffraction). A representative microstructure from an as-cooled Zr–8SS alloy shown in Fig. 4. The primary phase in this alloy is an α-Zr solid solution with ~95 atom% Zr and minor amounts of Fe, Cr, Ni, and other elements. The primary α-Zr phases are surrounded by a complex multi-phase matrix containing secondary α-Zr and $Zr_2(Fe,Ni)$, along with minor amounts of the $Zr(Fe,Cr)_2$ Laves phase.

Table 2
Composition of observed phases in zirconium–8 wt% stainless steel alloys [11,12] [a]

Phase	Crystal structure	Fe	Zr	Cr	Ni
α-Zr	Hexagonal close-packed	3	94	1.5	0.5
$Zr(Fe,Cr)_2$	AB_2 Laves phase	42	34	21	0
$Zr_2(Fe,Ni)$	$CuAl_2$-type	28	66	0	6

[a] Listed compositions are in at.% (±3%).

Even though the Fe–Zr diagram is not well established for Zr-rich compositions (note the dashed lines in Fig. 2), comparisons may be made between the alloy microstructure and the phase diagram predictions. Zirconium-rich SS–Zr alloys exhibit deviations from the Fe–Zr phase system. The phase diagram predicts primary α-Zr phases for a Zr–8Fe alloy, but it also predicts that the matrix intermetallic should be the Zr_3Fe compound instead of the observed multiphase mixture; Zr_3Fe is only a very minor constituent (less than ~5 vol%) in the multiphase mixture. Also, Zr_2Fe is a stable, high-temperature phase (above ~775°C), but $Zr_2(Fe,Ni)$ is dominant in the multiphase matrix in Fig. 4; Zr_2Ni is a stable compound in the Zr–Ni system. In addition, the Laves intermetallic, $Zr(Fe,Cr)_2$, would not be present in a Zr–8Fe alloy, but it is part of the multi-phase matrix in the Zr–8SS alloy.

3.3. Distribution of noble metals in SS–15Zr and Zr–8SS

Non-radioactive noble metal elements were used to represent the NMFPs in the waste form alloys. The pure

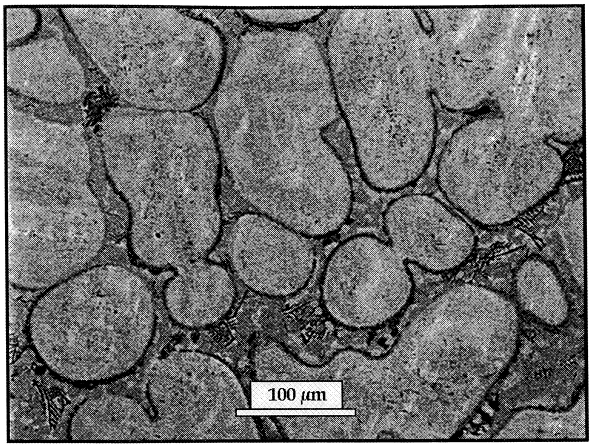

Fig. 4. Backscattered electron image of as-cooled zirconium–8 wt% stainless steel. The primary phase (bright) is α-Zr metal and the matrix phases comprise secondary α-Zr plus the $Zr(Fe,Cr)_2$ and $Zr_2(Fe,Ni)$ intermetallics.

metals Ru, Pd, Co, Nb, Ag, Re, Si, Ta and W were added to SS–15Zr and Zr–8SS alloys in the small- and large-scale samples; the noble metals Mn and Mo were present as components in 316 SS. The expected NMFP content in a 'real' waste form alloy is between 0.01 and ~4 wt%, depending on the burnup of the fuel being treated [11,12]. While most of the NMFPs are relatively short-lived radioactive isotopes, some isotopes have half-lives in the range of 10^5–10^7 years. For fast reactor fuel from EBR-II, computer simulations [3] show that the longest-lived NMFPs are ^{93}Zr ($t_{1/2} = 1.5 \times 10^6$ y), ^{99}Tc ($t_{1/2} = 2.13 \times 10^5$), and ^{94}Nb ($t_{1/2} = 2.0 \times 10^4$ y). In addition, the isotope ^{93}Nb ($t_{1/2} = 13.6$ y) is a significant decay product from ^{93}Zr that will be present for over 100 000 years.

Noble metal additions were made in combinations that totaled ~4 wt% per sample. For example, a typical noble metal addition to a SS–15Zr alloy was 2 Ru–1.5 Pd–0.5 Ag. In some cases, the non-radioactive additions were orders of magnitude greater than the expected NMFP levels, but the elevated concentrations were necessary to enable accurate EDS detection (e.g., the SS–15Zr waste forms from EBR-II will contain <0.01 wt% Ag, but typical Ag additions in these experiments were ~0.5 wt%).

No discrete noble metal phase were observed in the alloys, except for one case where Ag precipitates were found in an SS–15Zr alloy containing ~1 wt% Ag; in that instance a majority of the Ag was still in solution. Fig. 5 contains a set of X-ray maps highlighting the distribution of major components (Fe, Cr, Zr, and Ni) and selected noble metal components (Ru, Pd, Ag, and Mo) in an SS–15Zr microstructure. At the concentrations examined in this study, the noble metals are dissolved and distributed within alloy phases; the following data are expressed as atomic percent concentration ratios (intermetallic: α-Fe solution). The elements Si (~9:1), Nb (~8:1), Pd (~10:1), Ag (~5:1), Sn (~9:1), and Ta (~8:1) exhibit a strong preference for the intermetallics, and Ru (~4:1) exhibits a moderate preference. The elements Mn (~1:1), Co (~1:1), Mo (~1:1), Tc (~1:1) and W (~1:1) are found in the intermetallic and Fe solution phases without a strong preferential distribution.

Similar experiments have been carried out using Zr–8SS alloys; a typical noble metal addition to this alloy was 1Ru–1Pd–1Ag–1Nb (in wt%). The noble metal elements were dissolved in existing phases, but elevated concentrations were observed at α-Zr lath boundaries (Fig. 6); lath boundaries are α-Zr phase boundaries within the Zr phases in Zr–8SS. Keiser and McDeavitt [14] reported very similar lath morphologies in Zr–8SS alloys containing uranium and plutonium; elevated U and Pu concentrations were observed at α-Zr lath boundaries. This phase structure forms because the noble metals and actinides have a much higher solubility in β-Zr than in α-Zr [37]. During solidification the noble metals segregate to the α-Zr lath boundaries nucleated within prior β-Zr grains [38]. (The forthcoming data in Section 5 reveal that this segregation does not reduce the corrosion resistance of the alloys.) In addition, the element Pd also exhibited a strong preference for the $Zr_2(Ni,Fe)$ phase.

[3] ORIGEN computer simulation by R.N. Hill, Reactor Analysis Division, ANL.

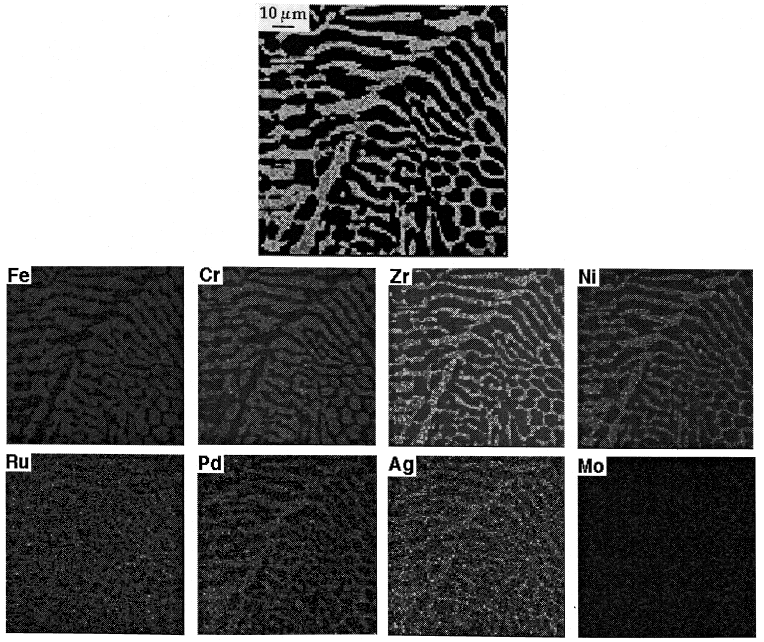

Fig. 5. Collection of X-ray maps and backscattered electron image of as-cooled stainless steel–15 wt% Zr–2 wt% Ru–1.5 wt% Pd–0.5 wt% Ag. The maps highlight the distribution of major (Fe, Cr, Zr, and Ni) and minor components (Ru, Pd, Ag, and Mo).

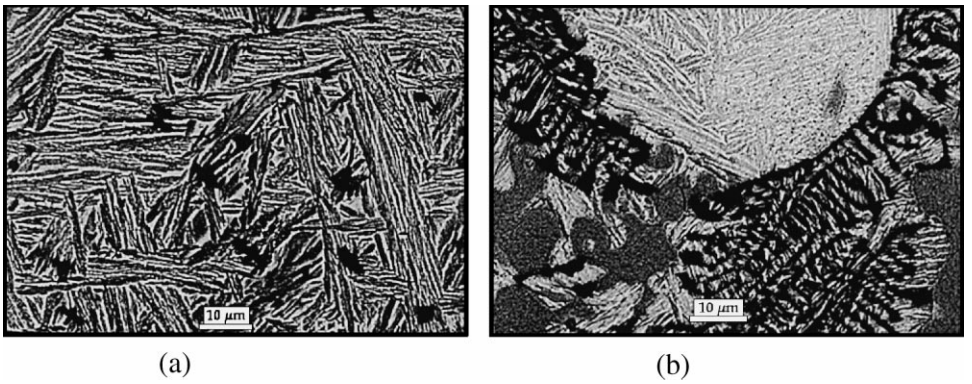

Fig. 6. Backscattered electron images of zirconium–8 wt% stainless steel–1 wt% Nb–1 wt% Ru–1 wt% Pd–1 wt% Ag. The noble metal content is enriched at Zr phase boundaries in (a) primary and (b) secondary zirconium phases.

4. Physical properties

Even though corrosion resistance and fission product retention are of primary importance to waste form performance, physical properties are also significant. Physical attribute measurements are required for waste form evaluation to provide relevant data for modeling waste form performance [2]. Mechanical and thermophysical properties of SS–15Zr and Zr–8SS alloys were measured using specimens machined from large-scale ingots generated in the tilt-pour casting furnace. Uniaxial tension tests (ASTM E8-96), impact tests (ASTM E23-96), and room-temperature density measurements (ASTM C 693) were carried out by ANL. Compression tests (ASTM E9-89) and additional tensile and impact tests were conducted by Westmoreland Mechanical Testing and Research, Inc. (Youngstown, PA). Temperature-dependent measurements (up to 900°C) of the density, thermal conductivity, coefficient of thermal expansion, and specific heat were made by the Thermophysical Properties Research Laboratory (West Lafayette, IN). Table 3 contains a compilation of the measured data along with comparable data for related metals (Type 316 stainless steel and zirconium) and

Table 3
Mechanical and thermophysical properties of SS–15Zr, Zr–8SS, and related materials

Property	SS–15Zr	Zr–8SS	Type 316SS [39]	Zirconium (>99.6%) [40]	Borosilicate Glass [c] [3]	Synroc [c] [3]
Ultimate tensile strength (MPa)	265 ± 10	255 ± 20	515	350–390	–	50–75
0.2% Yield stress (MPa)	a	a	275	250–310	–	–
Elastic modulus (GPa)	179 ± 8	87 ± 5	190	84.2	81–90	134–190
Tensile elongation (%)	<0.2	<0.2	~40	~25	–	–
Compressive strength (MPa)	1123 ± 30	1009 ± 30	–	–	–	574–810
0.2% Yield stress (MPa) (compression)	675 ± 10	343 ± 10	–	–	–	–
Elastic modulus (GPa) (compression)	180 ± 10	92 ± 10	–	–	–	288
Compressive strain (%)	7.5 ± 1	18 ± 1	–	–	–	–
Density @298 K (g/cm^3)	7.6 ± 0.1	6.6 ± 0.1	7.8	6.5	2.6	4.4
Thermal conductivity [b] (W/m K)	12.2	17.5	14.6	22.6	1.1	2.1
Coeff. of thermal expansion [b] (10^{-6}/K)	11	7.2	16.5	5.9	8.1	10.5
Specific heat [b] (J/g K)	0.45	0.30	0.5	0.29	0.9	0.55

[a] Failure typically occurred without measurable plastic deformation.
[b] Thermophysical property data are 'near room temperature' values.
[c] Data for glass and Synroc represent minimum and maximum reported values.

other waste form materials (borosilicate glass and Synroc).

As shown in Table 3, the ultimate tensile strength for SS–15Zr is comparable to the 0.2% yield strength for stainless steel, and that for Zr–8SS is comparable to the 0.2% yield strength for zirconium metal (99.6% purity). In addition, the elastic modulus for SS–15Zr is comparable to the modulus of 316SS, and the modulus for Zr–8SS is comparable to the modulus of zirconium metal. This implies that the metal solid solution phases in SS–15Zr (α-Fe in Fig. 1) and Zr–8SS (α-Zr in Fig. 4) dictate their elastic properties. The correspondence of the ultimate tensile strength in SS–15Zr and Zr–8SS with the yield stresses of 316SS and Zr implies that the onset of deformation in the metal phase (α-Fe of α-Zr) results in the subsequent fracture of the brittle intermetallic phases. The loss of intermetallic continuity reduces the load-bearing cross section over a very short time, increasing the load on the ductile metal phase and inducing rapid failure. In compression, the SS–15Zr and Zr–8SS alloys exhibit high values for the 0.2% yield stresses and ultimate compressive strength, and some plastic deformation occurs in both alloys prior to failure. This ductility difference in compression vs. tension in common in multi-phase materials, where one phase is ductile (e.g., a metal) and another phase is not (e.g., an intermetallic).

The density, thermal conductivity, coefficient of thermal expansion, and specific heat of SS–15Zr and Zr–8SS are comparable to those 316SS and zirconium, respectively. The primary differences between the metal waste form alloys and the glass and ceramic waste form materials are the density and thermal conductivity. The alloy densities are more than twice that of borosilicate glass. The higher thermal conductivity implies that the SS–Zr waste form alloys are capable of containing a significant quantity of radioactive (heat generating) waste elements while a relatively even temperature distribution is maintained. Thermal gradients and gradient-induced stresses that may induce fracture should not be as significant a problem for SS–15Zr and Zr–8SS; this is a significant contrast to the case for glass and ceramic waste forms [3,6].

5. Corrosion behavior

5.1. Immersion corrosion testing

The corrosion resistance of SS–15Zr and Zr–8SS alloys was tested using an immersion method and simulated groundwater, and preliminary data were presented by McDeavitt et al. [11–13]. The test procedure was based on MCC-1 (ASTM C 1220), a static leach test developed by the Materials Characterization Center (Hanford, WA) for glass-based waste forms. The procedure was modified to include alcohol washing of the alloy samples prior to immersion. The test involves exposing the sample to a static solution (e.g., simulated groundwater) for an extended duration (i.e., 3, 7, 28, or more days) at a fixed temperature of 90°C. The outcome of the test is evaluated by measuring changes in specimen mass and solution composition and, if possible, examining the alteration effects through metallographic analysis of the sample.

Disk-shaped specimens (16 mm diameter, 3 mm thick) were polished to better than a 200 grit finish, then immersed in the test solution in sealed Teflon vessels; the sealed vessels were placed in an oven at 90°C. The test solution was based upon the ionic composition of J-13

well water, which is representative of goundwater for the proposed high-level nuclear waste repository located at Yucca Mountain, Nevada. A representative composition of J-13 well water is (in mg/L): 11.5 Ca, 1.76 Mg, 45.0 Na, 5.3 K, 0.06 Li, 0.04 Fe, 0.001 Mn, 0.03 Al, 30.0 Si, 2.1 F^-, 6.4 Cl^-, 18.1 SO_4^{2-}, 10.1 NO_3^-, 143.0 HCO_3^-, and 5.7 dissolved oxygen [40].

Initial screening tests were carried out for SS–15Zr and Zr–8SS alloys, with and without noble metal additions. The initial test duration was 28 days, but no corrosion alteration was detected. After 10 000 h (417 d), only minimal surface alteration was visually evident on the test specimens; the metal surfaces were still very shiny except for a slight tarnish on a few samples. Mass changes were not detectable in any of the metal specimens. The differences between pre- and post-test masses were always within ±0.0001 g, which is within the resolution limit of the balance (±0.0001 g). Because of this minimal corrosion, solution chemistry changes and post-test metallography were not evaluated. Extended duration tests well beyond 10 000 h are underway.

5.2. Electrochemical corrosion testing

An electrochemical linear polarization test method (ASTM G59) was used to measure corrosion rates of SS–Zr alloys and other reference metals, and preliminary data were presented by McDeavitt et al. [11–13]. The test equipment consists of an electrochemical corrosion cell and a potentiostat. The experimental variables measured by this test method are the corrosion current density, i (mA/m^2), and the electrochemical overvoltage, n (V). The current density is measured during a controlled-potential scan with the following parameters: (a) range of potential scan = ±0.020 V of the pre-determined corrosion potential; (b) potential scan rate = 0.1 mV/s; (c) initial stabilization time = 0.5 h; and (d) initial delay time = 5 s. The data were converted into a corrosion rate using the Tafel relationship, $n = \pm B \log(i/i_0)$, and Faraday's law, $r = i_0/eF$ (where r is the calculated corrosion rate, i_0 is a reference current density at an equilibrium electrode, e the number of electrons transferred by the corrosion reaction, and B and F are constants). In the absence of mechanistic understanding, localized corrosion phenomena were neglected, and uniform corrosion was assumed.

The disk-shaped test specimens (16 mm diameter, 3 mm thick) were prepared in a similar manner to the immersion test specimens. A series of SS–Zr specimens with and without noble metals was prepared from small- and large-scale samples, and additional specimens were generated from commercial metals for comparison. The test solution was simulated groundwater (J-13 composition) at room temperature with additions to control the solution pH to 2, 4, 7, and 10; pH = 2 represents an extreme condition that may not occur naturally in the repository environment, but it provides an aggressive test for comparison of metals with low corrosion rates.

Measured corrosion rates for SS–15Zr and Zr–8SS alloys (with and without noble metals), commercial zirconium and stainless steels, and candidate waste canister metals are shown in Table 4 as a function of solution pH. The maximum measured corrosion rates for selected alloys are compared graphically in Fig. 7. The data ranges in Table 4 indicate minimum and maximum corrosion rates. The corrosion rates for the SS–15Zr and Zr–8SS alloys range between 0.3 and 12.7 μm/y. In both the SS–15Zr and Zr–8SS alloys, the noble metal additions do not significantly affect the measured corrosion rates of the waste form alloys. At pH = 7, the corrosion rates for SS–15Zr and Zr–8SS are similar to or slightly lower than the rates for Types 316 and 304 stainless steel and zirconium metal. At lower pH values, the SS–15Zr corrosion rates increase slightly (i.e., from 0.5 to 12.7 μm/y), similar to the trend measured for Types 316 and 304 stainless steel. The Zr–8SS rates re-

Table 4
Electrochemical corrosion rates of SS–Zr alloys and reference metals

Alloy (in wt%)	Corrosion rates (μm/y)			
	pH = 2	pH = 4	pH = 7	pH = 10
SS–15Zr	2.5–10.2	2.0–5.1	0.5–2.0	0.3–0.5
SS–15Zr–2Ru–1.5Pd–0.5Ag	10.2–12.7	5.1	1.0–2.5	1.5–2.3
Zr–8SS	0.5–2.0	1.3–1.5	0.5–0.8	0.3
Zr–8SS–1Ru–1Mo–0.5Pd	2.0	1.0	0.8	0.3
Zirconium	0.5	2.5	1.5–2.3	1.8
Type 304 SS	2.5	1.3	1.3	0.8
Type 316SS	7.6	1.3	1.0	0.8
Incoloy 825	0.8	1.3	1.8	0.8
Pure Cu (CDA122)	226	216	2.5–5.1	10.2
Cu–7Al (CDA614)	58	175	91	51
A106 Grade B low alloy steel	1270	584	305	305

Ranges indicate multiple data from similar specimens.

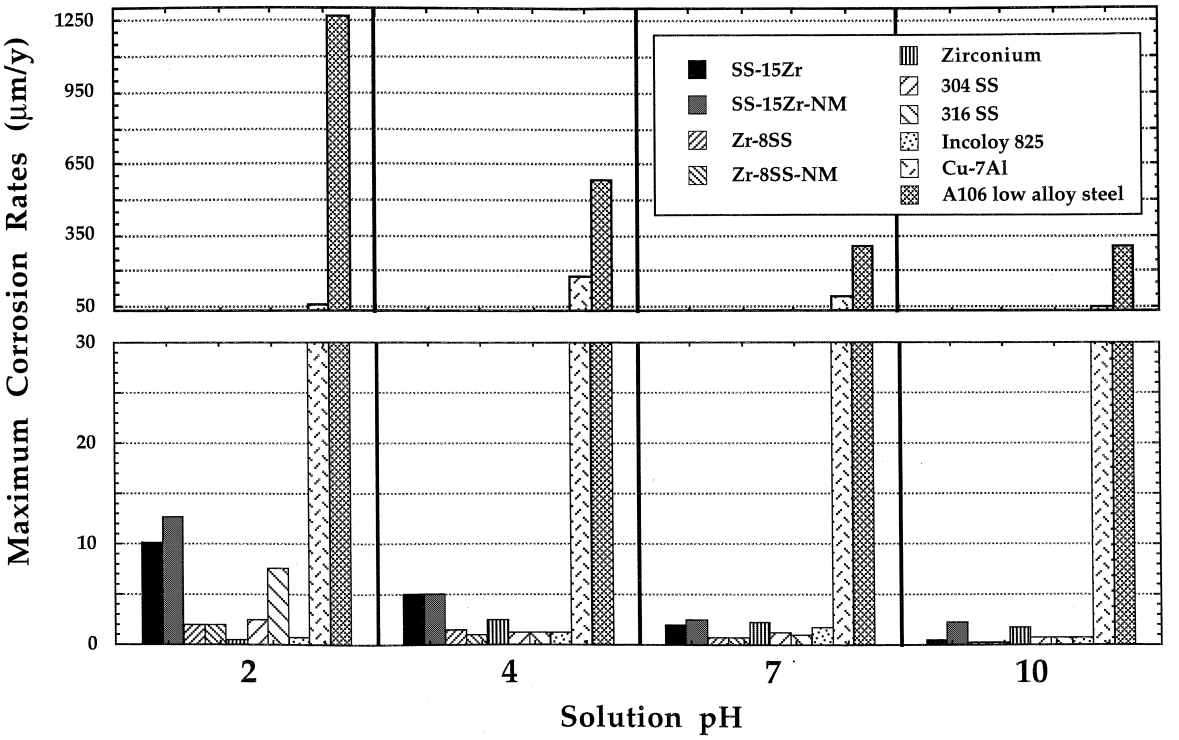

Fig. 7. Maximum corrosion rates from linear polarization experiments. The split-scale *y*-axis enables comparison between low and high corrosion rates [29].

main within the same order of magnitude (i.e., between 0.3 and 2.0 μm/y) for all pH solutions, similar to the trend observed for zirconium metal.

The Incoloy, copper alloys, and low-alloy steel specimens were included for comparison and illustrate the effectiveness of the linear polarization test in differentiating between the corrosion resistance of various types of metals. The measured SS–15Zr and Zr–8SS corrosion rates are also similar in magnitude to the rate for Incoloy 825, which is a corrosion-resistant metal that has been evaluated as a candidate material for nuclear waste canisters. The measured SS–15Zr and Zr–8SS corrosion rates are one to two orders of magnitude below the rate for pure copper (CDA122) and Cu–7 wt% Al (CDA614), and two to three orders of magnitude below the rate for low alloy steel (A106 Grade B). These metals have also been considered for waste canister application where the metal would be designed to corrode in service.

5.3. Accelerated corrosion testing

The purpose of an accelerated test is to generate long-term alteration (i.e., corrosion) in a short time through increasing the alteration rate without changing the nature of the alteration mechanism [2]. Acceleration may be accomplished in various ways, such as increasing the test temperature or increasing the specimen surface area. Caution is necessary when interpreting accelerated test results because the accelerated alteration mechanism may differ from that at lower temperature [2].

The vapor hydration test is an accelerated test developed to measure the chemical durability of glass waste forms under severe conditions [42], and it has proven useful for testing SS–Zr waste form alloys. In this test, disk-shaped monolith specimens (16 mm diameter, 3 mm thick) with notches are suspended by a Teflon wire in a sealed stainless steel container that also contains a small pool of water beneath the specimen. The sealed vessel is heated to 200°C, and the water vaporizes to create condensation and evaporation of water on the test specimen. The sealed test assembly is held in this condition for 28 to over 300 days.

Waste form durability is measured as a function of (a) the thickness of the surface reaction layer, or alteration layer, and (b) the amount and nature of secondary phases formed on specimen surfaces. Fig. 8(a) and (b) show post-test optical photos of SS–15Zr and Zr–8SS specimens, respectively, following a 56-day exposure at 200°C. The alloy surfaces were oxidized, but severe degradation was not evident. The specimen edges were still very sharp, and the alteration layers were <1 μm in

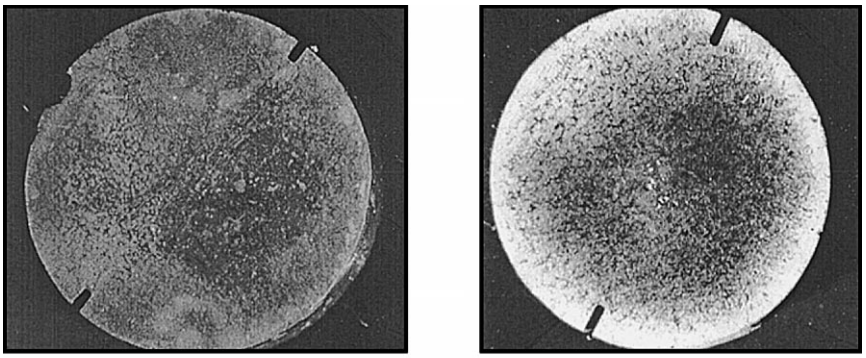

Fig. 8. Optical photos of (a) SS–15Zr and (b) Zr–8SS samples after 56 days in vapor hydration test. Minor alteration is evident in the shape retention of the specimen.

thickness. The specimens were cross-sectioned and examined by electron microscopy, but the thin alteration layers were not observable by SEM. X-ray diffraction revealed that hematite (Fe_2O_3) was present on the SS–15Zr alloy, and baddeleyite (monoclinic ZrO_2) was present on the Zr–8SS alloy.

In contrast, some borosilicate glass and other ceramic-based waste materials form a significant amount of crystalline secondary phases and have alteration layers up to 300 μm thick under similar conditions [43–45]. The standard glass used for enviromental assessment (EA glass) comparisons when qualifying glass waste forms for disposal has been tested with this method. The EA glass is completely converted to crystalline powder after only 3 days in vapor hydration tests at 200°C, although EA glass is not representative of a superior glass waste form [43]. Representative glass waste forms (e.g., SRL-165 and SRL-202) exhibit relatively high durability with alteration layers between 50 and 200 μm thick after 56 days at 200°C [43,44]. Therefore, the durability of the SS–Zr waste form alloys in saturated water vapor may be considered superior to all waste glass materials for which data are available.

6. Discussion: SS–15Zr and Zr–8SS as nuclear waste forms

The physical property data in Table 3 indicate that SS–15Zr and Zr–8SS are physically sufficient to be waste form materials. The primary implication of this data is that SS–15Zr and Zr–8SS are very strong, with mechanical and thermophysical properties that are comparable to other metals. The physical demands on a waste form are relatively insignificant as compared to the requirements for corrosion resistance and fission product retention. Waste forms are not load bearing or structural materials; they must simply reside in a waste canister for a very long time. In other words, the mechanical and thermophysical properties itemized in Table 3 will not inhibit the repository performance of SS–15Zr and Zr–8SS. In fact, their high strength and excellent thermal properties are very favourable for a waste form.

Both alloys exhibit a solubility for noble metal elements in their microstructures. In SS–15Zr (Fig. 1), all of the noble metals tested in this study are soluble to some degree in the $Zr(Fe,Cr,Ni)_{2+x}$ intermetallic phase, and some of them (Mn, Co, Mo, Sn, W, and Re) are also soluble in the Fe solution phase. Therefore, the $Zr(Fe,Cr,Ni)_{2+x}$ phase plays a significant role in immobilizing the noble metal fission products in SS–15Zr. In Zr–8SS (Fig. 4), there is evidence that a portion of the noble metals may segregate to interphase boundaries within the α-Zr phases, but the primary component in these noble metal-rich boundaries is still zirconium. The immersion and electrochemical corrosion data indicate that the addition of noble metals does not significantly alter their corrosion behavior in either alloy, despite the segregation noted in Zr–8SS. The primary conclusion from these observations is that the noble metals are well-entrained in SS–15Zr and Zr–8SS such that the fission product release rate in both alloys will be controlled by the corrosion behavior of the alloy matrix phases.

In light of that conclusion, groundwater corrosion resistance is a primary performance indicator for the SS–Zr waste form alloys. The immersion tests show that the J-13 groundwater solution is very benign to the SS–Zr alloys, and that this type of test is not aggressive enough to quantify the corrosion rate. Because of the robust nature of the waste form materials and the negligible corrosion that was observed, the test solutions were not analyzed to detect leaching of the simulated fission products. It is evident from the MCC-1 data, however, that a short-term immersion test is not especially useful as a quantitative tool in the long-term

evaluation of corrosion resistance or leach resistance for the alloys.

The electrochemical linear polarization data (Table 4, Fig. 7) quantitatively confirm that the corrosion rates in simulated groundwater are indeed very low. The highest corrosion rate measured for an SS–Zr waste form alloy was 12.7 μm/y (SS–15Zr–4NM), and that was measured at the unrealistic groundwater pH = 2. The natural pH of J-13 groundwater is typically on the order of 7–9. A typical corrosion rate at pH = 7 was ~1 μm/y, which would extrapolate to ~1 mm of alteration after 1000 years. Unfortunately, the numbers generated by the electrochemical method have limited accuracy because of the mechanistic assumptions that are made to convert the corrosion current and potential measurements into a corrosion rate. Therefore, even though the precision of the data is very good (i.e., the data from this method are reproducible), and the corrosion rates of the SS–Zr alloys are verified to be very low, these results cannot be translated into a reliable long-term prediction.

On the other hand, the vapor hydration results provide a direct assessment of the long-term durability of SS–15Zr and Zr–8SS. This accelerated method was used to evaluate the nature and extent of the relevant alteration mechanisms following a procedure that has been used to evaluate the durability of glass waste forms. The fact that the alteration was negligible (i.e., <1 μm in 56 days) shows, again, that these alloys are very corrosion resistant. The observation of trace amounts of Fe_3O_4 on SS–15Zr and ZrO_2 on Zr–8SS reveals, as might be expected, that oxidation is a primary alteration mechanism. The negligible alteration confirms that the oxidation rate is extremely low. Similar vapor hydration experiments (200°C, 56 days) on pure Cu and Fe resulted in dramatic alteration, which suggests that the Cr and Zr in the alloys provide corrosion protection through the formation of an oxide passivation layer.

An inherent difficulty in waste form evaluation, for any waste form material, is that long-term behavior predictions must be based on short-term data, and the accuracy of these predictions is limited if the corrosion mechanism is not well understood. Any extrapolation of corrosion rates (e.g., ~1 μm/y to ~1 mm at 1000 y) or linkage of test methods (e.g., electrochemical rates to vapor hydration rates) must be done with extreme caution. However, since waste forms must contain their radioactive constituents for thousands or millions of years, such extrapolations are tempting. There is a significant jeopardy in this because no method exists to validate the underlying assumptions behind extrapolations to 1000 years or 1 million years.

However, the present corrosion data shows that SS–15Zr and Zr–8SS are very corrosion resistant, even under stringent short-term test conditions. Moreover, while long-term behavior predictions are not practicable, the metal waste form alloys compare exceedingly well with established waste form materials such as borosilicate glass and Synroc [3–8,43–45]. Therefore, it may be concluded that these metal alloys are viable waste forms for their defined application.

7. Summary and conclusions

Stainless steel–15 wt% zirconium and zirconium–8 wt% stainless steel alloys were generated in high-temperature, inert-atmosphere furnaces at 1600°C. Both small- and large-scale samples were prepared, and test specimens were machined from the cast materials. The characterization data reported above were generated to substantiate the selection of SS–15Zr and Zr–8SS as waste forms and to provide a reference database for the continued development and eventual qualification of these waste form materials for repository application. From the above results, it is apparent that SS–15Zr and Zr–8SS are viable waste form materials that may be used to immobilize metallic wastes for geologic disposal.

The following conclusions are evident from this work.

1. The metallurgy of SS–15Zr and Zr–8SS is now well established, especially for SS–15Zr, which has been examined more completely than Zr–8SS because of the electrometallurgical process demonstration underway with stainless steel-clad fuel from the EBR-II reactor.

2. Simulated fission product elements are distributed in solution in the intermetallic and metal solution phases of the SS–15Zr alloy. The noble metals are also in solution in the Zr–8SS phases, but elevated concentrations are observed at lath boundaries in α-Zr.

3. The Laves intermetallic phase in SS–15Zr, $Zr(Fe,Cr,Ni)_{2+x}$, plays a significant role in the retention of NMFPs. Without the zirconium, this phase would not form, and some of the noble metals (e.g., Nb, Pd, and Ag) might not be well-incorporated in the alloy microstructure.

4. The mechanical and thermophysical properties of SS–15Zr and Zr–8SS demonstrate that the alloys are mechanically strong and exhibit thermal properties comparable to other metals. This demonstrates that SS–15Zr and Zr–8SS are more than adequate, physically, for waste form application.

5. Immersion tests in simulated groundwater at 90°C are very benign to SS–15Zr and Zr–8SS, with and without noble metals. The alloys are very resistant to this environment, and negligible corrosion was observed. Short-term immersion testing is not useful for quantitative evaluation of the long-term corrosion rate or leach resistance.

6. The electrochemical linear polarization tests verify that the corrosion rates of SS–15Zr and Zr–8SS are very low. The corrosion rates for these alloys are comparable to other corrosion-resistant metals, such as

Type 316 stainless steel, zirconium metal, and Incoloy 825.

7. Vapor hydration tests demonstrated that SS–15Zr and Zr–8SS are very durable materials. Minimal corrosion was observed on both alloys after 56 days, even though similar conditions significantly alter glass and ceramic waste form materials.

8. The SS–15Zr and Zr–8SS waste form alloys have the potential for acceptance as non-standard materials for use as high-level nuclear waste forms.[41]

Acknowledgements

The authors would like to acknowledge J.P. Ackerman, L.J. Simpson, D.D. Keiser, Jr., D.J. Wronkiewicz, R.N. Hill, J.W. Richardson, B.S. Tani, J.K. Basco, and L.E. Putty for their supporting efforts in this work. This work was supported by U.S Department of Energy under contract W-31-109-Eng-38.

References

[1] L.J. Jardine, J.J. Laidler, Qualifying radioactive waste forms for geologic disposal, Lawrence Livermore National Laboratory Report, UCRL-JC-118385, 1994.
[2] Standard Practice for Prediction of the Long-Term Behavior of Waste Package Materials Including Waste Forms Used in the Geologic Disposal of High-Level Nuclear Waste, ASTM Standard Practice C 1174, 1991.
[3] W. Lutze, R.C. Ewing, Radioactive Waste Forms for the Future, North-Holland, Amsterdam, 1988.
[4] I.W. Donald, B.L. Metcalfe, R.N.J. Taylor, J. Mater. Sci. 32 (1997) 5851.
[5] J.J. Cunnane, High-level waste borosilicate glass, A compendium of corrosion characteristics, US Department of Energy Report, DOE-EM-0177, 1994.
[6] Hj. Matzke, E. Vernaz, J. Nucl. Mater. 201 (1993) 295.
[7] W.L. Ebert, The effects of the glass surface area/solution volume ratio on glass corrosion: A critical review, Argonne National Laboratory Report, ANL-94/34, 1995.
[8] A.J.G. Ellison, J.J. Mazer, W.L. Ebert, Effect of glass composition on waste form durability: A critical review, Argonne National Laboratory Report, ANL-94/28, 1994.
[9] S.M. McDeavitt, J.Y. Park, J.P. Ackerman, in: B. Mishra, W.A. Averill (Eds.), Actinide Processing: Methods and Materials, The Minerals, Metals, and Materials Society, Warrendale, PA, 1994, p. 305.
[10] D.P. Abraham, S.M. McDeavitt, J.Y. Park, Metall. Mater. Trans. A 27A (1996) 2151.
[11] S.M. McDeavitt, D.P. Abraham, D.D. Keiser, Jr., J.Y. Park, in: International Topical Meeting on Nuclear and Hazardous Waste Management, vol. 3, American Nuclear Society, LaGrange Park, IL, 1996, p. 2477.
[12] S.M. McDeavitt, D.P. Abraham, D.D. Keiser, Jr., J.Y. Park, in: V. Ramachandran, C.C. Nesbitt (Eds.), Extraction and Processing for the Treatment and Minimization of Wastes, The Minerals, Metals, and Materials Society, Warrendale, PA, 1996, p. 177.
[13] D.P. Abraham, S.M. McDeavitt, J.Y. Park, in: DOE Spent Nuclear Fuel and Fissile Material Management, American Nuclear Society, LaGrange Park, IL, 1996, p. 123.
[14] D.D. Keiser, Jr., S.M. McDeavitt, in: DOE Spent Nuclear Fuel and Fissile Material Management, American Nuclear Society, LaGrange Park, IL, 1996, p. 123.
[15] J.J. Laidler, J.E. Battles, W.E. Miller, J.P. Ackerman, E.L. Carls, Prog. Nucl. Eng. 31 (1997) 131.
[16] J.P. Ackerman, Ind. Eng. Chem. Res. 30 (1991) 29.
[17] J.E. Battles, J.J. Laidler, C.C. McPheeters, W.E. Miller, in: B. Mishra, W.A. Averill (Eds.), Actinide Processing: Methods and Materials, The Minerals, Metals, and Materials Society, Warrendale, Pennsylvania, 1994) p.135.
[18] E.C. Gay, W.E. Miller, in: Proceedings of DOE Spent Nuclear Fuel Challenges and Initiatives, American Nuclear society, LaGrange Park, IL, 1994, p. 267.
[19] J.J. Laidler, E.C. Gay, in: International Topical Meeting on Nuclear and Hazardous Waste Management, vol. 3, American Nuclear Society, LaGrange Park, IL, 1996, p. 2432.
[20] K.M. Goff, R.W. Benedict, K. Bateman, M.A. Lewis, C. Pereira, C.A. Musick, in: International Topical Meeting on Nuclear and Hazardous Waste Management, vol. 3, American Nuclear Society, LaGrange Park, IL, 1996, p. 2436.
[21] J.P. Ackerman, T.R. Johnson, L.S. Chow, E.L. Carls, W.H. Hannum, J.J. Laidler, Prog. Nucl. Eng. 31 (1997) 141.
[22] J.P. Ackerman, L.S.H. Chow, S.M. McDeavitt, C. Pereira, R.H. Woodman, JOM 49 (1997) 26.
[23] M.A. Lewis, D.F. Fischer, C.D. Murphy, Mater. Res. Soc. Symp. Proc. 333 (1994) 95.
[24] C. Pereira, M.C. Hash, M.A. Lewis, M.K. Richmann, JOM 49 (1997) 34.
[25] M.C. Hash, C. Pereira, M.A. Lewis, R.J. Blaskovitz, J.P. Ackerman, in: Environmental and Waste Management Issues in the Ceramic Industry-II, American Ceramic Society, Westerville, OH, 1996, p. 135.
[26] F. Pacaud, C. Fillet, N. Jacquet-Francillion, Mater. Res. Soc. Symp. Proc. 251 (1992) 161.
[27] X. Feng, D.J. Wronkiewicz, J.K. Bates, N.R. Brown, E.C, Buck, M. Gong, W.L. Ebert, in: R.G. Post (Ed.), Waste Management'94, Laser Options, Inc., Tucson, AZ, 1994, p. 1541.
[28] J. Broothearts, F. Casteels, A. Daniels, P. DeRegge, D. Huys, A. Leurs, Conditioning of cladding waste by compaction and encapsulation in low-melting metal alloys, Commission of the European Communities Report, EUR 9670, 1985.
[29] S.M. McDeavitt, D.P. Abraham, J.Y. Park, D.D. Keiser Jr., JOM 49 (1997) 29.
[30] D.P. Abraham, J.W. Richardson, S.M. McDeavitt, Scr. Mater. 37 (1997) 239.
[31] D.P. Abraham, J.W. Richardson, S.M. McDeavitt, Mater. Sci. Eng. A 239–240 (1997) 658.
[32] D. Arias, M.S. Granovsky, J.P. Abriata, in: H. Okamoto (Ed.), Phase Diagrams of Binary Iron Alloys, ASM International, Materials Park, OH, 1993, p. 467.

[33] F. Laves, Theory of Alloy Phases, ASM, Cleveland, OH, 1956, p. 123.
[34] R.L. Berry, G.V. Raynor, Acta Crystallogr. 6 (1953) 178.
[35] Y. Komura, Acta Crystallogr. 15 (1962) 770.
[36] Y. Liu, S.M. Allen, J.D. Livingston, Scr. Metall. Mater. 32 (1995) 1129.
[37] T.P. Massalski (Ed.), Binary Alloy Phase Diagrams, ASM International, Materials park, OH, 1990.
[38] G. Ökvist, K. Kälström, J. Nucl. Mater. 35 (1970) 316.
[39] J.R. Davis (Ed.), Stainless Steels, ASM International, Materials Park, OH, 1994.
[40] E.A. Brandes, G.B. Brook (Eds.), Smithells Metals Reference Book, Butterworth-Heinemann, Linacre House, Jordan Hill, Oxford, 1992.
[41] A.E. Ogard, J.F. Kerrisk, Groundwater chemistry along flow paths between a proposed repository site and the accessible environment, Los Alamos National Laboratory Report, LA-10188-MS, 1984.
[42] J.K. Bates, M.G. Seitz, M.J. Steindler, Nuclear and Chemical Waste Management 5 (1984) 63.
[43] J.K. Bates et al., ANL technical support program for DOE office of environmental management: Annual report (October 1994–September 1995), Argonne National Laboratory Report, ANL-96/11, 1996.
[44] W.L. Ebert, J.K. Bates, Mater. Res. Soc. Symp. Proc. 176 (1990) 339.
[45] D.J. Wronkiewicz, L.M. Wang, J.K. Bates, B.S. Tani, Mater. Res. Soc. Symp. Proc. 294 (1993) 183.